



Role of silicon on formation and growth of intermetallic phases during rapid Fe–Zn alloying reaction

Seung-Chang Han ^a, Dario Ferreira Sanchez ^b, Daniel Grolimund ^b, Sang-Ho Uhm ^b, Du-Youl Choi ^c, Hong-Chul Jeong ^c, Tea-Sung Jun ^{a, d, *}

^a Department of Mechanical Engineering, Incheon National University, Incheon, 22012, Republic of Korea

^b Swiss Light Source, Paul Scherrer Institut, CH-5232, Villigen PSI, Switzerland

^c Welding and Joining Research Group, Steel Solution Marketing Department, POSCO, Incheon, 21985, Republic of Korea

^d Research Institute for Engineering and Technology, Incheon National University, Incheon, 22012, Republic of Korea

ARTICLE INFO

Article history:

Received 13 February 2023

Received in revised form

4 April 2023

Accepted 14 April 2023

Available online xxx

Keywords:

In-situ synchrotron XRD

Advanced high strength steel

Alloying elements

Zn coating

Fe–Zn reaction

Intermetallic phase

ABSTRACT

The study of liquid metal embrittlement in Fe–Zn systems is challenging because of the high temperature and vapor pressure of Zn, which hinders *in-situ* investigations with sufficiently high spatial resolution. This is typically associated with subsecond processing steps and the coexistence of a solid substrate and a liquid Zn phase, which renders direct observations at the microstructural scale difficult. In this study, we comprehensively investigate the reactions occurring during the rapid heating and cooling stages of Fe–Zn systems using synchrotron X-ray diffraction. The phase transformation is analyzed for specimens with different interfacial structures, with focus on changes in the coating microstructure above and below the peritectic temperature (782 °C) of the Fe–Zn system. Advanced high-strength steel (AHSS) variants with 1.5 wt% Si content show a prominent destabilizing effect at the onset of Fe–Zn intermetallic compound formation and a simultaneous deceleration of the liquid Zn depletion rate compared with other AHSS alloys containing 0 wt% Si. Furthermore, the addition of Si suppresses the formation of the Γ phase, which is due to turbulence in the outburst Zn at temperatures above 773 K. Consequently, the fraction of Γ phase compounds with accumulated Zn decreases as the exposure time of the liquid Zn to the ferritic matrix increases owing to the solute redistribution of Si in the liquid Zn during rapid heating. Meanwhile, the absence of silicon in the substrate causes the formation of a ζ phase with a low melting point, which delays the formation of liquid Zn via an increase in the melting point of the Zn layer in the early stage of heating. Additionally, the amount of residual liquid Zn decreases due to the rapid depletion of Zn during the liquid initiation stage via an equilibrium Fe/Zn binary phase transformation. The results of this study provide a deeper understanding of the Fe–Zn intermetallic phase transformation and the sensitivity to liquid metal embrittlement of third-generation AHSSs based on silicon content.

© 2023 The Authors. Published by Elsevier Ltd. This is an open access article under the CC BY license (<http://creativecommons.org/licenses/by/4.0/>).

1. Introduction

Unique challenges to fuel economy and safety standards in the automotive industry have resulted in the necessity for high-performance structural materials with formability levels that satisfy component manufacturing requirements. Third-generation advanced high-strength steels (AHSSs) are of interest in this aspect; hence, significant weight savings and corrosion resistance

have been focused on alloy design. The application of an integral Zn-based galvanized coating on the surface of AHSS sheets is essential for increasing the service life of vehicle structures against corrosion. Resistance spot-welding (RSW) is challenging because the AHSS sheets involved exhibits a temperature sufficient to melt the Zn-coated layer on the surface, and thermo–mechanical-induced tensile stresses occur simultaneously. However, third-generation AHSS grades with strengths exceeding 1000 MPa pose a high risk during RSW owing to the application of a sacrificial Zn or Zn–Fe layer on the surface. During RSW, high temperatures are attained by the Zn-coated AHSS sheets, causing the Zn-coated layer on the AHSS surface to melt. This results in the formation of

* Corresponding author. Department of Mechanical Engineering, Incheon National University, Incheon, 22012, Republic of Korea.

E-mail address: t.jun@inu.ac.kr (T.-S. Jun).

intergranular cracks that are larger than 100 μm on the wetted surfaces. When liquid and solid phases coexist, the infiltration of the liquid phase reduces the cohesive strength of the matrix grain boundaries. Ductile metals are not protected against embrittlement when they are exposed to a liquid metal for only a fraction of a second [1–5].

Grain boundaries contribute significantly to polycrystalline materials, which are typically affected by intergranular degradation phenomena, such as stress corrosion cracking [6–8], hydrogen embrittlement [9–11], and liquid metal embrittlement (LME) [12–14]. Furthermore, hot working processes (i.e., hot press forming [15–18] and resistance spot welding [19–22]) are associated with the rapidity of microscopic processes and drastic temperature changes, thus rendering temperature monitoring and control extremely difficult. These processes are different from the conventional heat treatment, as rapid heating and cooling do not allow the temperature profiles to reach a steady state. The transient nature of rapid heating involving melting and rapid cooling in these processes can result in the formation of non-equilibrium intermetallic compounds (IMCs). Because the phase transformation is accompanied by turbulence due to the outburst Zn at peritectic temperatures (773–1073 K) [23], an increasing fraction of these compounds with accumulated Zn reduces the exposure time of the liquid phase on the ferritic matrix. To provide more insights into the inhibition of LME and the related nanoscopic microstructural changes in the Fe–Zn system, these phenomena should be investigated at a small scale. The effect of silicon content on AHSSs has only been investigated phenomenologically without knowledge regarding the chemical properties of each intermetallic phase; hence, further detailed studies are required.

Previous studies have explicitly considered the role of silicon content in enhancing the formation of Fe–Zn IMCs; however, they lacked experimental observation [24–27]. The presence of alloying elements (such as Sn, Sb, P, S, and Si) in a galvanizing bath or the chemical composition of AHSS has been shown to affect the non-uniform Fe–Zn reaction, thus resulting in increased amounts of liquid Zn available to cause LME. Recent studies suggest that grain boundary chemistry-induced alterations in the atomic-binding strength result in grain boundary decohesion. Owing to the complexity of the interactions between subsecond processing steps and the coexistence times of the solid–liquid phase, no comprehensive framework for the intermetallic phase transition or their relationship pertaining to the existence of silicon content has been established hitherto. Therefore, direct observations should be conducted, and the mechanism by which silicon affects interfacial reactions should be clarified.

Hence, in this study, we characterize the nucleation of intermetallic phases and their subsequent growth based on *in-situ* investigations at high spatial resolutions. Laser heating induces phase transition, and two-dimensional X-ray diffraction analysis reveals the properties of the transient state, which shows a specified time delay. Recent developments in ultrafast detectors and the high flux provided by third-generation synchrotron radiation sources have facilitated experiments with timescale resolutions relevant for laser-based industrial implementations. Using the combined experimental methodology, we aim to perform a study that correlates the thermodynamic and kinetic parameters of the Fe–Zn system by altering the composition of the steel substrate with different concentrations of silicon in AHSS. The growth of the intermetallic phase and the onset of phase transition during laser scanning are elucidated and discussed.

The objective of this study is to explore the impact of silicon as an alloying element on the formation and growth of intermetallic reaction layers at the interface between a Zn coating layer and AHSS at elevated temperatures during thermal processing. Controlled

experiments are conducted to compare the reactions between the Zn coating layer and AHSS with and without silicon as an alloying element, both above and below the peritectic temperature of the Fe–Zn binary system. The approach provides evidence that the nucleation and growth of intermetallic phases during rapid solidification are dependent on the concentration of silicon as an alloying element. Specifically, our findings suggest that silicon decelerates the formation of a uniform and solidified Γ Fe–Zn intermetallic phase at the interface between the coating and substrate, while also increasing the overall amount of liquid zinc. This finding presents an alternative origin to the previously discussed mechanisms described in the literature.

2. Methods

2.1. Materials

Industrially produced third-generation galvanized AHSS sheets with a tensile strength of 1180 MPa was cold rolled by an identical amount to a final thickness of 1.6 mm. The nominal chemical composition of the third-generation transformation-induced plasticity (TRIP) steel is Fe–2.6Mn–0.7C, with variation in the concentration of silicon (Table 1). The cold-rolled TRIP steel sheets were intercritically annealed to induce variations in the retained austenite phase. Steel sheets with different chemical compositions were coated with a $\sim 10\text{-}\mu\text{m}$ -thick zinc layer via hot-dip galvanization in a Zn–0.2 wt% Al bath, whereby, in general, the steels can be corrosion resistant owing to the adherent Zn-coated layer. More details regarding the selective oxidation and galvanizing processes are available in the literature [28]. Rectangular samples (10 mm \times 10 mm \times 1.5 mm) rectangular samples were cut from the samples via electro-discharged machining (EDM).

2.2. Experimental set-up

The experimental setup at the micro-X-ray absorption spectroscopy beamline of the Swiss Light Source (SLS) includes a laser beam, laser beam dumps, a pyrometer, and *in-situ* synchrotron micro-focused X-ray diffraction, as shown in Fig. 2(a). An X-ray focal spot with a full width at half maximum (FWHM) of $40\text{ }\mu\text{m} \times 40\text{ }\mu\text{m}$ was generated using a Si (111) monochromator and Kirkpatrick–Baez mirror optics. Monochromatic incident beam passed through the near-center of the sample and $\alpha\text{-Al}_2\text{O}_3$ was used as a calibration standard. Photon energy of 17.2 keV (corresponding to a wavelength of 0.7208 Å) was used to allow for the measurement of a sufficient number of diffraction peaks of the Zn and α -Fe phases without overlap.

A copper holder was custom developed to be used as a support and link between the sample and stage. The samples were horizontally fixed on the hole of the copper heat-sink stage, with a

Table 1
Chemical composition (wt.%) of TRIP 1180 samples.

	C	Mn	Si	P	S	Fe
GI-1.5Si	0.17	2.6	1.5	0.008	0.002	Balance
GI-0Si	0.17	2.6	—	0.008	0.002	

The microstructural characterization was carried out using Zeiss AXIO scope and JEOL JSM-7800F field emission scanning electron microscopy (SEM). Fig. 1 presents the SEM micrograph of the samples with a silicon concentration of 1.5 wt% (hereinafter referred to as GI-1.5Si) and 0 wt% (hereinafter referred to as GI-0Si). The micrograph clearly confirms that the steel microstructure is composed of (bainitic) ferrite and martensite–austenite (labeled as α and M/A, respectively). Notably, both C and Mn are austenite-stabilizing elements, whereas silicon is rejected from carbide precipitation and serves as a barrier for further growth during intercritical annealing.

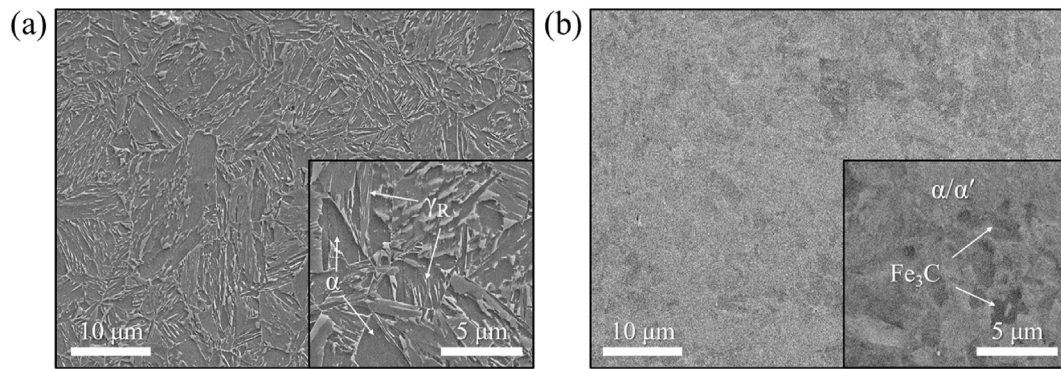


Fig. 1. SEM micrograph of third-generation AHSS microstructure of AHSS (a) GI-1.5Si (1.5 wt% Si); (b) GI-0Si (0 wt% Si). α , α' , γ_R , and Fe_3C represent (bainitic) ferrite, martensite, retained austenite and cementite, respectively.

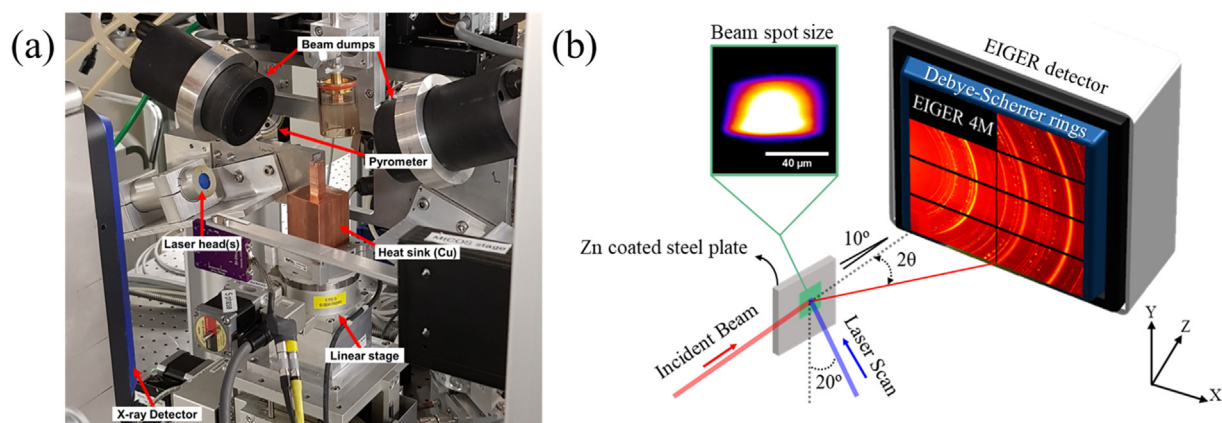


Fig. 2. (a) Experimental setup for in-situ micro X-ray diffraction experiments, with laser system mounted on Micro-XAS beamline (X05DA port of the SLS). (b) Schematic illustration of the laser system mounted on the Micro-XAS beamline (X05DA port of the SLS). For scale, the sample shown in (a) is 1.6 mm thick.

glancing angle of 10° to the sample surface. Fig. 2(b) illustrates the outline of the sample, laser heating, and *in-situ* X-ray diffraction systems. The direct beam was aligned with the module border and shielded by a beam stop. In the experimental setup, the reflection mode is required by the materials deposited on top of the surfaces or below them with respect to the primary beam as well as to set the incidence angle. An incidence angle of 10° allows the penetration depth of the X-ray beam to be varied below the sample surface and to probe the surface of the sample or interfaces far below it.

As a laser source, two near-infrared diode lasers (Apollo Instruments, USA [29]) with a heating capacity of 150 W were inclined 20° to the sample, by which the laser beam passing through the sample can be absorbed via water-cooled beam dumps. Both sides of the samples were laser heated using two diode lasers with a laser beam profile measuring $1\text{ mm} \times 1\text{ mm}$. The samples were simultaneously cooled using a Cu heat sink during laser heating and rapidly quenched at the end of heating. Such an approach mimics the heating–cooling system of RSW.

2.3. Data analysis

Local microstructures undergo an order–disorder transition within a short time because of high heating/cooling rates (up to $10^6\text{ }^\circ\text{C/s}$). Thus, a high acquisition rate is mandatory to observe rapid solidification and ordering within a short time. To capture these phenomena, a rapid X-ray detector with submillisecond time resolution is required, and background noise must be minimized.

The experiments reported herein can be conducted using EIGER X-ray detectors with an energy threshold to appropriately synchronize the detector with the laser operation. The diffracted photons were recorded on an EIGER $\times 4\text{ M}$ single-photon counting detector (Dectris, Switzerland) with a total active area of 2070×2167 pixels at a pixel size of $75\text{ }\mu\text{m}$. The detector was operated at a continuous frame rate of 750 Hz, with an exposure time of 15 ms for each frame. The detector was placed away from the sample to maximize the 2θ resolution while optimizing the range of the reciprocal space. Two-dimensional (2D) diffractograms recorded by the EIGER $\times 4\text{ M}$ system were screened at the beamline for quality control using the ALBULA viewer (Dectris, Switzerland). Detector distance calibration, background subtraction, azimuthal integration, and averaging were performed using XRDUA v7.1.3.1 [30]. All diffractions were converted from q to 2θ using an in-house Python script, based on $q = 4\pi \cdot \sin\theta/\lambda$, where q is the scattering vector (momentum transfer), 2θ the diffraction angle, and λ the X-ray wavelength. A series of 2D diffraction patterns was azimuthally integrated into the one-dimensional (1D) diffraction profiles. The background was integrated in the range $11 < q < 60\text{ nm}^{-1}$ and then subtracted. To distinguish the signal from the liquid phase and systematic background, the background determined at 12,000 ms was utilized as the specimen was fully solidified at that time. The systematic background produced by the beam optics and setup was assumed to remain constant throughout the experiment owing to the high beam stability provided by the SLS. The integrated peak intensities, peak positions, and lattice strains were obtained from the least-squares fitting of Gaussian functions to the 1D

diffraction patterns at every point in time. Lattice strains were calculated from the planar distance, where $d = 2 \cdot \pi / q$. The analysis and plotting of X-ray diffraction and imaging were performed using Python (Anaconda distribution, Continuum Analytics, USA) combined with IPython [31], matplotlib [32], SciPy and NumPy packages [33]. Perceptually uniform color maps were retrieved from the Cmocean package [34].

2.4. Temperature evolution

Temperature control was achieved through a direct definition of the laser current profiles at the measured temperature. A pyrometer targeted at the surface of a workpiece was used to estimate the mean temperature evolution near the X-ray beam position. Whereas pyrometers are typically restricted to a narrow wavelength window and provide only an integrated temperature value over the full spot size, the evolution of the d-spacing can provide temperature variations associated with local temperature gradients. The critical transformation temperatures (A_{c1} , A_{c3} , M_s , and M_f) for the steel were determined using dilatometry, as shown in Fig. 3(a). Because the melting and boiling points of Zn ($T_m = 419^\circ\text{C}$ and $T_b = 907^\circ\text{C}$) are low compared with those of Fe ($T_m = 1538^\circ\text{C}$ and $T_b = 2862^\circ\text{C}$), the temperature variance can be obtained for each experimental result (lattice parameter) using the coefficients of thermal expansion (CTE) (see in Fig. 3(b)). The temperature evolution presented in Fig. 3(c) is based on the estimated lattice parameter and dilatometry of Fe(110). The temperature was estimated from the lattice parameters using the CTE correlation for α -Fe at temperatures lower than that for γ -Fe [35]. The local temperature of the surface as a function of the CTE can be expressed as follows:

$$T(d) = T_R + 302.7 + 719.3 \times CTE - 57.8 \times TLE^2$$

where T_R is the room temperature, and time $t = 0$ denotes the onset of the laser pulse. The peaks associated with the crystalline coating layer vanished after approximately 1 s. As the reaction occurred in less than half a minute, heating with a time scale of less than 5 s is essential for understanding the phenomena. A temperature between the peritectic temperatures of the δ phase (672°C) and Γ phase (782°C) was selected because the temperature attained at the LME-sensitive locations of the spot welds might be subcritical temperatures (e.g., 500°C – 750°C) [36,37].

3. Results and discussion

3.1. Phase transformation during laser melting processing

The GI-1.5Si and GI-0Si samples were gradually heated for 3 s to

achieve full Zn coating melting. Raw images of Debye–Scherrer rings captured by the EIGER detector before and after laser heating are shown in Fig. 4 (a) and (b). The figures show two frames selected from the sequence of time-resolved diffraction patterns, which display the overall phase evolution during melting and solidification. In fact, μ -XRD can be used to probe the entire coating layer η , which allows clear Debye–Scherrer rings for the (110), (200), and (211) α -Fe planes in the matrix to be observed. The fraction of the incident beam was larger than that of the coating layer, and the initial coating contained the η phase. Any difference in the Fe–Zn alloying reactions between the GI-1.5Si and GI-0Si samples during this time period will directly reflect the effect of silicon at elevated temperatures. Moreover, several spots within the (110) ring of the GI-1.5Si sample revealed the existence of nanoscale fine grains in Fe–Zn intermetallic phases. This suggests a contribution to diffraction from an intermetallic phase (Γ -nanograins) that has formed near the (110) ring; however, the signal was extremely weak owing to the small scattering volume with a fine particle size. Intermetallic compounds (IMCs) can be generated by the abrupt development of Fe–Zn phases owing to Fe and Zn interdiffusion through the inhibition layer. However, nanoscale IMCs can be generated by the formation of small amounts of Si-rich particles inside liquid Zn during heating, thus resulting in the limited activation of Fe and Zn interdiffusion. Alternatively, rapid quenching in the liquid state can limit the diffusion time and result in the formation of competing phases. Similar effects can be expected owing to rapid heating; however, most studies pertaining to hot deformation cracking involving the interdiffusion of chemical samples have been performed isothermally or at moderate heating rates [22,24,25,38,39]. However, Fig. 4 (b) shows that GI-0Si is composed of stable intermetallic layers in the same range of diffraction angles. Based on the fully solidified diffraction pattern in Fig. 4 (a) and (b), the intermetallic phases formed entirely between the intermetallic Fe and Zn phases, including $\text{FeZn}_{13}(\zeta)$ ($c12/m1$) [40], $\text{Fe}_{13}\text{Zn}_{126}(\delta)$ ($P6_3/mmc$) [41,42], $\text{Fe}_{22}\text{Zn}_{78}(\Gamma_1)$ ($F\bar{4}3m$) [43], $\text{Fe}_3\text{Zn}_{10}(\Gamma)$ ($I\bar{4}3m$) [42]. The phases are composed of an Fe–Zn intermetallic phase in the range of $26 < q < 31 \text{ nm}^{-1}$. The 2D diffractogram characterizes the ordering reactions between Fe and Zn with different silicon concentrations in the AHSS substrate, which directly affect the interaction between the liquid and AHSS substrate during rapid heating and cooling.

In Fig. 4 (c) and (d), the 1D diffraction data before and after the onset of solidification are shown in the range of $15 < 2\theta < 40$. All the XRD spectra of the Zn coating exhibited predominant (101) reflection at $2\theta = 19.9^\circ$, along with the (002), (100), (102), (013), and (112) characteristic peaks originating from 2θ values of 16.8° , 18.0° , 24.7° , 31.2° , and 35.8° , respectively, which corresponds to the η -phase with a hexagonal structure ($P6_3/mmc$). The resulting diffraction data for different silicon contents show strong

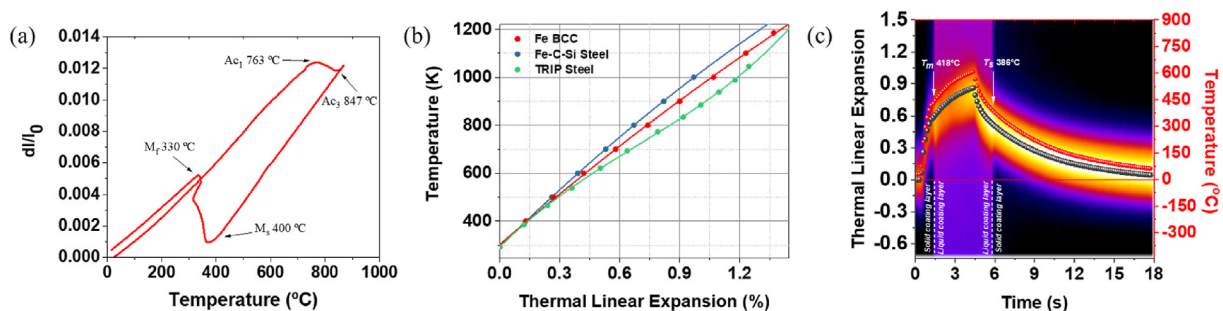


Fig. 3. Temperature can be obtained for each XRD pattern using calculated thermal expansion coefficients. More precise values of the actual thermal linear expansion of the third-generation AHSS are extremely important for temperature calculation. (a) Dilatation response during heating and cooling cycles of TRIP 1180. (b) Expansion/contraction of volume of unit cell arising from the temperature variation. (c) Representative lattice parameter and temperature variation of α -Fe (110) phase.

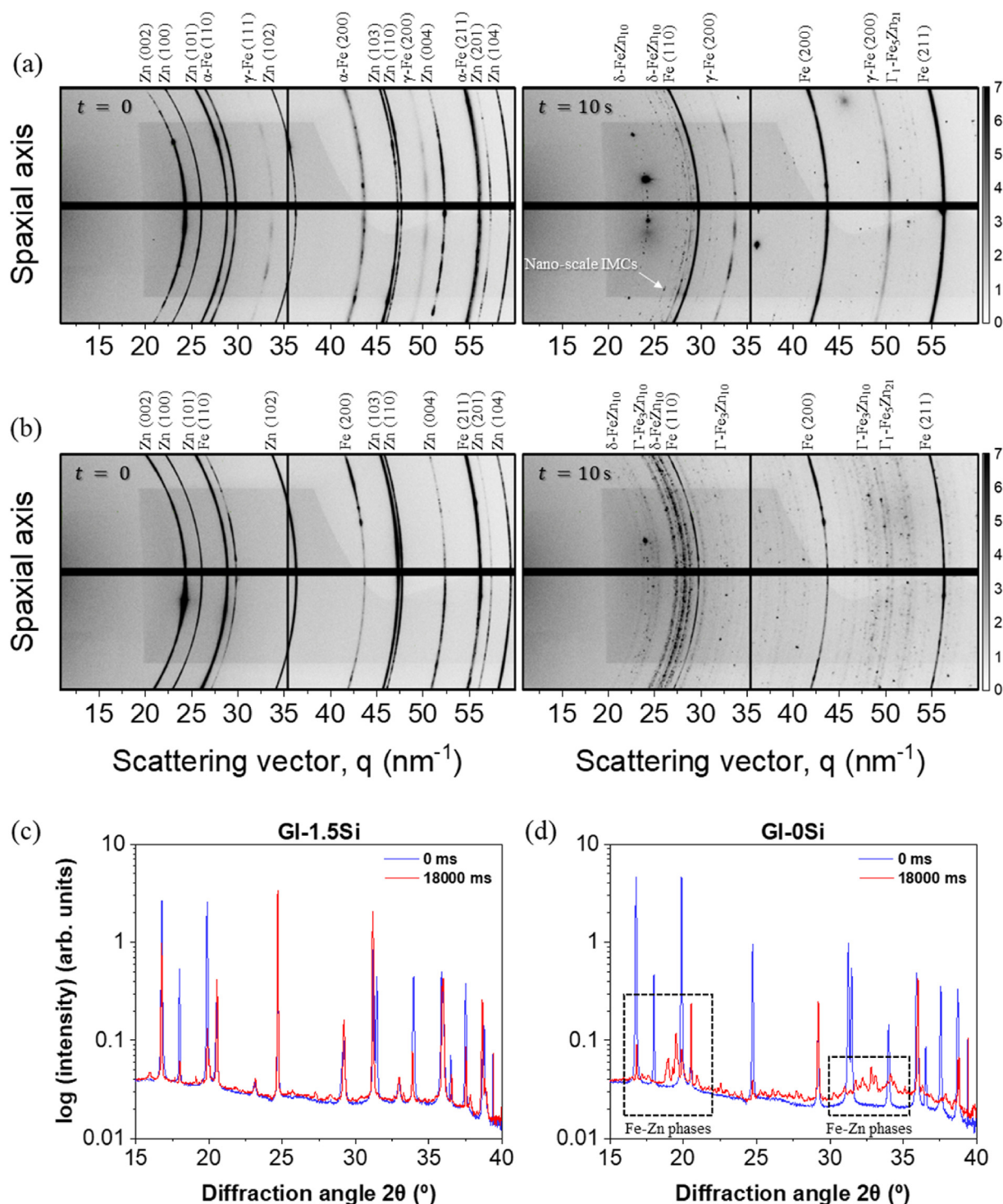


Fig. 4. Full q dependence shown by azimuthally integrating each measured 2D image to obtain XRD profile curves before laser scan ($t = 0$) and fully cooled ($t = 10$) of (a) GI-1.5Si and (b) GI-0Si. Representative in-situ x-ray diffraction data obtained from diffraction patterns recorded prior to laser scan and fully cooled samples of (c) GI-1.5Si and (d) GI-0Si.

dependency on the concentration. In GI-0Si, Fe–Zn intermetallic layers formed at the interface between solid Fe and liquid Zn at the early stage of heating and subsequently developed to $\text{Fe}_{13}\text{Zn}_{126}$ (δ), $\text{Fe}_{22}\text{Zn}_{78}$ (Γ_1), and $\text{Fe}_3\text{Zn}_{10}$ (Γ) phases after cooling. In GI-1.5Si, the presence of silicon exerted a prominent delaying effect on the ordering kinetics by reacting with liquid Zn before it can react with steel, in which case the Fe–Al inhibition layer can affect the transformation. The significant decrease in the intensity of the Zn reflections indicates order loss at relatively fast disorder kinetics.

The reaction sequence during heating to 700°C and subsequent cooling can be clearly visualized via a stacked diffractogram contour plot. Fig. 5 shows the azimuthally integrated XRD patterns that summarize the sequentially arranged diffraction profiles as a function of time. Laser heating was performed at an amplitude of 90 A for 3 s. The X-ray intensity for each 2θ angle at a specific time is represented by each point on the contour plot. In both the GI-1.5Si and GI-0Si samples, the diffraction lines disappeared and were replaced by a broad peak from the liquid phase when the Zn coating

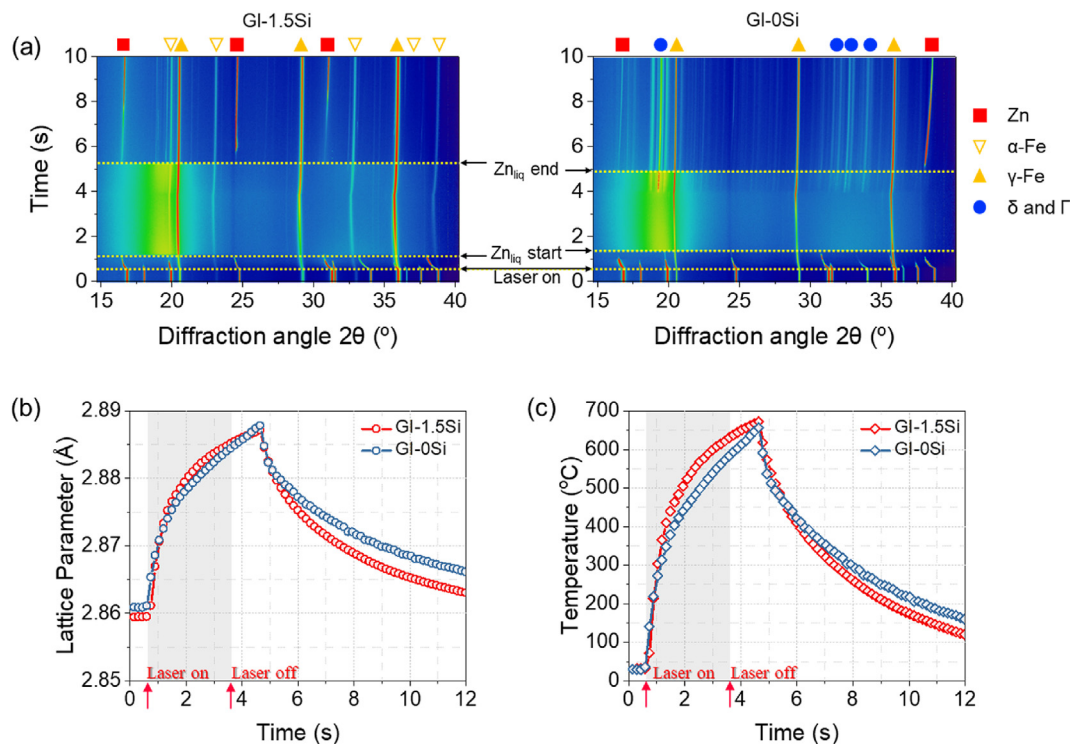


Fig. 5. (a) Time series of recorded 2D diffractograms provide information about the phase evolution from the initial state to the subsequent cooling state. (b) Comparison of the lattice parameter of the α -Fe(110) and temperature profile as a function of time for the GI-1.5Si and GI-0Si samples.

melted. When the laser was turned off (at $t = 1.8$ s), the solidifying material resulted in diffraction peaks, thus allowing the sequence of phases from the melting temperature to room temperature to be observed. The peaks for the η and ζ phases vanished during the heating phase, and the remaining α -Fe matrix peaks abruptly shifted to lower angles owing to thermal expansion. Upon solidification, α -Fe formed thicker lines and shifted to higher angles owing to thermal contraction. The time resolution during the experiment was 15 ms. However, in the GI-0Si sample, the Γ -Fe₃Zn₁₀ phase formed first, followed by δ -FeZn₁₀ and Γ -Fe₅Zn₂₁. The full range of the δ and Γ phase peaks was evident and revealed a fine-grained nature. The reaction kinetics can be limited by silicon diffusion into the lattice, causing the formation of the Γ -Fe₃Zn₁₀ phase first on the surface, followed by that of δ -FeZn₁₀ and Γ -Fe₅Zn₂₁. This outcome may not be immediately evident from the Fe–Zn binary equilibrium phase diagram, which favors the formation of both δ and ζ phases at higher temperatures and a greater Zn supply. The intensity of the α -Fe(110) peak increased significantly and intermittently before decreasing. While the intensity decreased, the signal of the IMCs became intermittent, which is attributable to crystallite movement in the liquid phase. Meanwhile, the result for GI-1.5Si confirmed that the crystals of the ζ phase were not heterogeneously nucleated at the liquid Zn/steel interface when the steel substrate contained a high amount of Si. This implies that the presence of silicon in the liquid state is transferred from the substrate and triggers a non-equilibrium state in Fe/Zn.

A summary of the results obtained during the heating experiments is shown in Fig. 5 (b) and (c). The lattice parameters and temperature profiles of the α -Fe(110) peak are presented as a function of time. Based on the analysis of the data described in Section 2, the precise temperatures of the phase transformations were determined based on plots showing the lattice parameter evolution of α -Fe(110) at certain 2θ angles. The result shows that

silicon changed the lattice parameter of α -Fe because the substitutional solution of silicon contracted the ferritic lattice, as shown in Fig. 5 (b). The lattice parameters of solid solutions depended mainly on the solute type and concentration. Silicon is one of the less abundant substitutional solutes that degrades the lattice parameters of steel. These results suggest that the supersaturated silicon on α -Fe in the early stage of heating can reduce the driving force for the nucleation of Fe–Zn phases and thermodynamically destabilized binary systems [27].

To investigate the effect of silicon content on the alloying of Fe–Zn, the phase evolution of the Zn coating during the hot-working process must be investigated. The trends clearly show that the Fe–Zn alloying reaction correlates with the silicon content at temperatures below the peritectic point when the substrate is mainly ferritic/martensitic (BCC/BCT). However, silicon can affect the Fe–Zn alloying reaction at temperatures above the peritectic point when the substrate is primarily austenitic (FCC). Fig. 6 presents representative diffractograms showing the change in the phase transformation mechanism in the presence and absence of liquid Zn and Si, respectively. Laser heating was performed at an amplitude of 80 A for 5 s to increase the peak temperature.

In the case of GI-0Si, the δ phase formed first, followed by the Γ phase. The δ phase that appeared during heating formed as the main phase when the reaction temperature was between 485 °C and 672 °C. The increased diffraction intensity and slight decrease in 2θ reveal ordering from the amorphous liquid to the δ phase. This primary δ phase coexisted with the liquid upon solidification and was observed intermittently before stabilizing. The main δ phase appeared to be coarse grained based on the low recorded intensity of only a few grains, which fulfilled the diffraction condition. The growth rate of the δ and Γ phases indicates that the δ phase resulted in a low growth rate because the δ phase was rapidly consumed during heating to form the Γ phase; in this regard, the melting point was 782 °C. However, the case for GI-1.5Si was

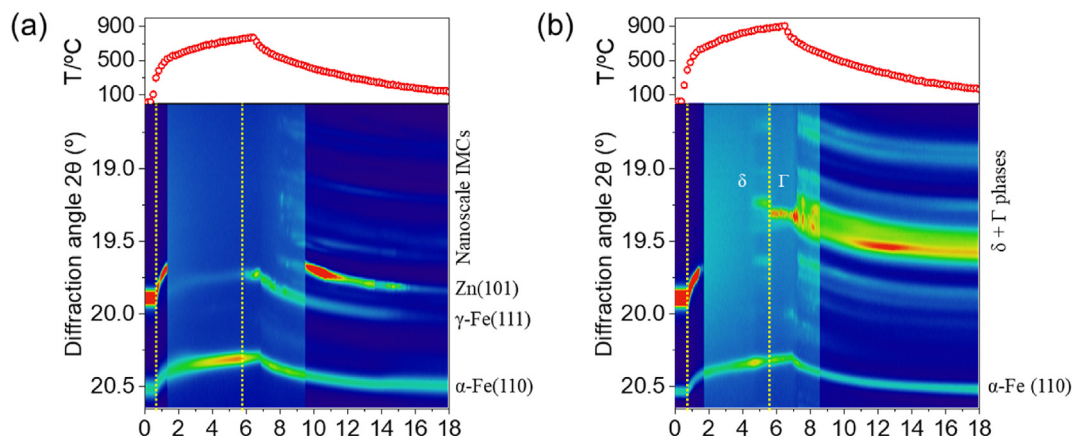


Fig. 6. Transition of Fe–Zn alloying reaction shown by azimuthally integrating each measured 2D image to obtain XRD profile curves (a) GI-1.5Si (b) GI-0Si. The material is subjected to laser heat treatments with a heating time of 5 s.

different, i.e., Zn was fully transformed into small amounts of Γ and δ during the subsequent cooling. The phase sequence of the Zn layer during heating was as follows: initial $\eta \rightarrow$ Zn melt $\rightarrow \delta +$ liquid $\rightarrow \delta + \Gamma +$ liquid, whereas during cooling, α -Fe(Zn) + solidification $\Gamma +$ decomposition $\delta + \Gamma_1$. The intensity of the α -Fe(110) peak increased significantly and intermittently before decreasing. While the intensity was decreasing, the signal of the δ phase became intermittent, which is attributable to crystallite movement in the liquid phase. At temperatures above the peritectic reaction temperature, the temperature at which the change from α -Fe to γ -Fe occurs is important to determine the amount of Fe that can be included in the intermetallic phase. GI-1.5Si only causes Fe thermal expansion, whereas GI-0Si results in a decrease in intensity owing to its participation in the intermetallic phases. The activation energy can be reduced significantly owing to the low interfacial energies of the nucleus when considering heterogeneous nucleation at the interface of the two existing phases. Consequently, the energy barrier for Γ nucleation at the coherent δ/α -Fe interface should be extremely low. Hence, only a small amount of Γ phase is formed after solidification in GI-1.5Si. Cho et al. reported that no orientation relationships were indicated between α -Fe and each of Γ , Γ_1 , and Γ_2 , as well as between the Γ_1 and δ phases during the galvannealing of a Mn–Si TRIP steel [44]. In the case of GI-1.5 Si, the nucleation of the Γ phase is hindered because an orientation relationship is not indicated between the δ phases, which results in a higher activation energy for nucleation. This can be attributed to the redistribution of solute atoms such as Si, which have low solubility in the Γ phase [45,46]. The accumulation of solute atoms at the interface changes the interfacial energy.

A detailed analysis of the peak evolution shows the coexistence of the liquid phase and α -Fe(110) upon solidification (cf. Fig. 6). Before the lasers were shut off, the α -Fe(110) peaks increased rapidly. Fe atoms expanded thermally and diffused rapidly through the amorphous ζ -phase film to form a compact intermetallic layer. However, in the GI-1.5Si sample, the crystals of the ζ phase were not heterogeneously nucleated at the liquid Zn/steel interface. Upon heating, the liquid Zn became saturated with Si, which was restrictively dissolved in the Fe–Zn phase, thus promoting FeSi segregation and increasing the α -Fe intensity. As shown in Fig. 6, only nanoscale fine IMCs were formed. The phase evolution of the initial Zn coating during the thermal cycle involved Zn melting, the formation of a Zn–Fe intermetallic layer, and a solid solution comprising α -Fe and Zn. The structure of the coating during the high-temperature phase development was affected by its silicon content. The results suggest that adding silicon to a steel substrate

causes FeSi crystal segregation in the early stage of heating and retards Fe–Zn phase formation owing to difficulty in nucleating the ζ phase due to silicon redistribution.

The reactivity of Fe and Zn on a steel substrate depends on the ability of the solute atoms to segregate at the grain boundaries. Elements that form compounds and precipitate at the grain interiors result in clean grain boundaries, and the formation is not hindered by the intermetallic phase [23]. The results of the present study confirm that the addition of silicon as an alloying element reduces the nucleation of the δ phase. This implies that the silicon concentration changes in a manner similar to the Fe–Zn phase transformation. The phase evolution of the initial Zn coating included Zn melting, the formation of a Zn–Fe intermetallic layer, and α -Fe with Zn in the solid solution of the reacted coating during the thermal cycle. The coating structures corresponding to high-temperature phase development were affected by the silicon content. The results obtained suggest that the addition of silicon to a steel substrate segregates the FeSi crystal in the early stage of heating, and that the retardation of the Fe–Zn phase formation is caused by the difficulty in nucleating the ζ phase owing to the redistribution of the solute Si. Su et al. found that even small amounts of silicon dissolved in the liquid dramatically reduce Fe solubility in liquid Zn [47,48].

Fig. 7(a)–(d) shows the phase evolution of the Zn towards the ζ phase prior to the formation of fully liquid Zn. Before the IMCs can form during cooling, Zn must first rapidly diffuse into the matrix. In such a scenario, the phase transformation related to the initiation of liquid Zn is dominated by chemical changes due to Zn diffusion into the boundary, whereas our observations clearly indicate the nucleation and growth of intermetallic phases. Based on our observations, we propose a sequence of intermetallic formations during the early stage of the heating process, which comprises the steps schematically summarized in Fig. 7(e).

Fig. 7(e) shows the expected trajectory of the melting point in a Fe–Zn system, where the binding of Zn to an intermetallic causes significant change to the melting temperature of the η layer, which depends on the size or growth time of Fe–Zn. The intensity of the Zn reflections decreased rapidly at 438 °C, indicating the initiation of liquefaction at a temperature above the melting point of pure Zn (420 °C). Notably, the phase transformation is a first-order transformation and generates latent heat. During this transformation, the system either absorbs or releases a significant amount of energy per volume, and the temperature remains constant as heat is added [49]. Phase transformations typically occur through reversible structural fluctuations between disordered and crystalline states

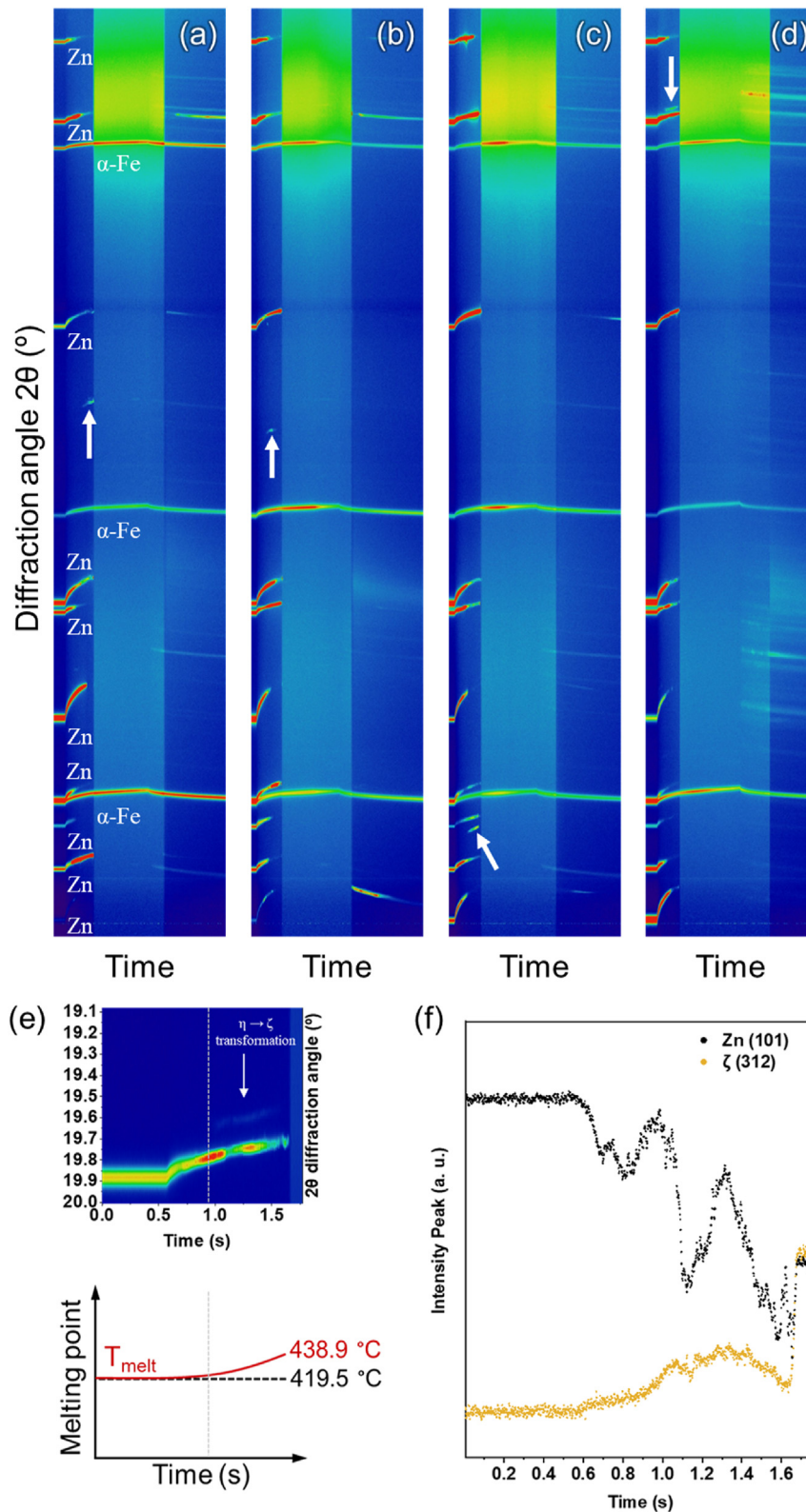


Fig. 7. Phase evolution of the integrated diffraction pattern in the early stage of heating. A resulting phase evolution of GI-OSi was shown as a diffraction angle 2θ vs. time stitched plot of 15 ms segments. The sample was cyclically heated and cooled using increasing laser current with (a) 60A (b) 70A (c) 80A and (d) 90A. The white arrow in the diffraction image indicates the formation of an intermitted ζ phase followed by $\eta \rightarrow \zeta$ transformation. (e) Melting temperature change of a nucleus as a function of its growth time. A nucleus can have a melting temperature lower than its reaction temperature owing to melting point depression. (f) Intensity fluctuations in the early stage of heating. Dynamics of azimuthally integrated Zn(101) and ζ (312) profiles and structural fluctuations in the early stage of crystallization.

[50]. The experimental results supporting this hypothesis are shown in Fig. 7 (f). Notably, the onset of liquid zinc formation was delayed during the initial formation of the Fe–Zn intermetallic. As previously mentioned, silicon occupies vacancies in the Fe–Al compounds, thus increasing the barrier effect. The nucleation of the ζ phase prior to the complete formation of the liquid state can only be detected in the GI-0Si sample. A few Si-rich particles were formed in the Zn-coated layer, and no other intermediate phases were observed in GI-1.5Si. These results show that the growth of

the Zn layer can be substantially suppressed by the addition of Si. The amount of Zn was limited by the rate at which it was supplied through grain boundary diffusion, which creates an Fe-rich local environment and reduces the driving force for the nucleation and growth of the Γ intermetallic phase. Meanwhile, GI-0Si can decrease the absolute time of the residual liquid Zn owing to the formation of intermetallic (ζ phase) during the early stage of heating and the rapid depletion of Zn caused by intermetallic formation (Γ phase), which can be directly related to the sensitivity of

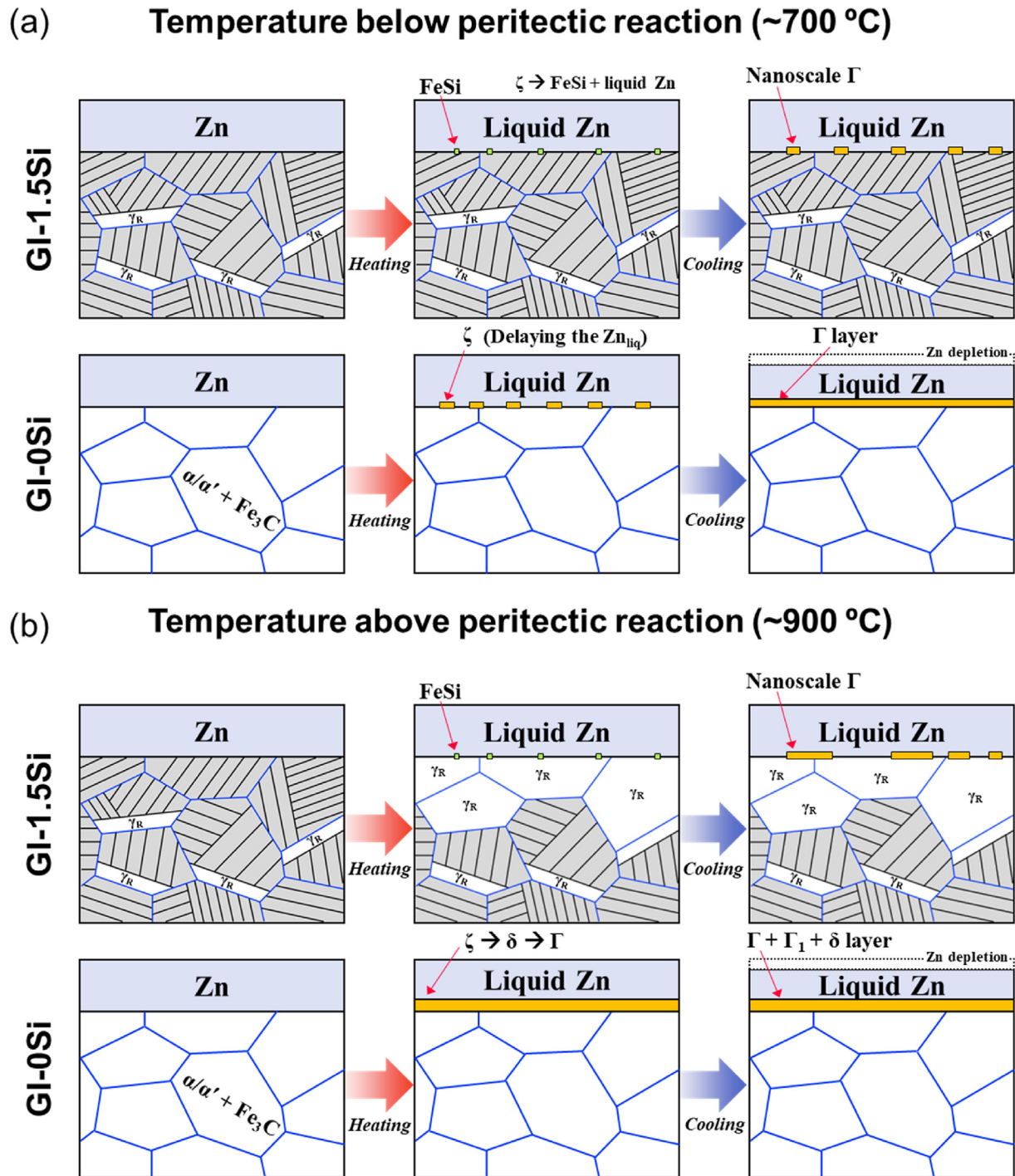


Fig. 8. Schematic representation of the effect of silicon content on Fe–Zn alloying reaction and its microstructural evolution based on data obtained at temperatures (a) below the peritectic reaction (~700 °C) and (b) above the peritectic reaction (900 °C). (For interpretation of the references to color in this figure legend, the reader is referred to the Web version of this article.)

LME. These intermetallic phases appear to represent the heating stage of the Fe–Zn alloying reaction; therefore, strategies to limit Zn diffusion into the Fe–Zn binary system or suppress the nucleation and growth of the intermetallic phase are crucial to prevent mechanical degradation (i.e., LME) in the next generation of AHSSs.

The findings presented in Figs. 4, Fig. 5, Figs. 6 and 7 support the hypothesis that the absence of silicon promotes the nucleation of the ζ phase prior to Zn melting and accelerates the formation of a uniform and solidified Γ Fe–Zn intermetallic phase at the coating/substrate interface, resulting in a reduction of the overall amount of liquid Zn. Based on the present observations, we now propose a sequence of the Fe–Zn alloying reaction based on the presence and absence of silicon concentration in the steel substrate. The steps are schematically summarized in Fig. 8.

It should be noted that the Fe–Zn system comprises various intermetallic phases and Fe and Zn are mutually soluble in one another. However, the addition of silicon creates a conducive environment in the Fe(solid)/Zn(liquid) system. At temperatures below the peritectic temperature (782 °C) in the Fe–Zn system, the diffusion of Si into liquid Zn hinders the formation of the Fe–Zn intermetallic phase at the interface between solid Fe and liquid Zn. (refer to Fig. 8 (a)). In this temperature range of approximately 500 °C, the ζ phase could solidify from the liquid as Fe diffuses into the coating. In GI-1.5Si, the intermetallic (ζ) phase is thermodynamically destabilized and replaced by the ferrite and liquid Zn phases as silicon is increasingly added to the liquid Zn. At an elevated temperature, the Fe concentration of Zn penetration in GI-0Si is enough to reach the solubility limit, and the liquid solidifies into Γ phase. In 1.5Si, the Fe dissolution is insufficient to drive Fe–Zn intermetallic phase formation.

At elevated temperatures above the peritectic temperature (782 °C), the Si concentration in the steel substrate influences the uniformity and thickness of the intermetallic layer at the Fe(solid)/Zn(liquid) interface (refer to Fig. 8 (b)). In the GI-1.5Si coating, a small proportion of the nano-scale intermetallic phase, Γ , is generated above the interface due to the delaying effect of Si on Fe dissolution. Consequently, liquid Zn can freely come into contact with the steel substrate in the GI-1.5Si coating. In contrast, in the GI-0Si coating, the Fe-saturated liquid alloy transforms into the $\zeta \rightarrow \delta \rightarrow \Gamma$ phases, which begin to form from the liquid Zn state, and Fe becomes highly concentrated during solidification below the peritectic temperature of Γ . The driving force for Γ phase transformation is enough to homogeneously nucleate the Γ phase. During solidification, after the laser is turned off, the Γ phase is replaced by the Γ_1 and δ phases, forming uniform intermetallic layers that effectively prevent direct contact between liquid zinc and the susceptible matrix. However, the addition of Si leads to a reduction in the intermetallic phases (ζ , δ , and Γ), and this destabilizing effect of Si on the Fe–Zn intermetallic phase explains the absence of the Γ phase and increased liquid Zn fraction in the reacted coating of the GI-1.5Si. It is worth noting that the Si-rich α -Fe(Zn) appears to be generated after complete solidification.

For the application of advanced high-strength steels (AHSS), which typically contain Si as an alloying element, it is crucial to understand the impact of Si content on the Fe–Zn alloying reaction. Additionally, surface treatment (i.e., decarbonization) or micro-alloying can be explored as a means of mitigating Zn-induced embrittlement, which could be related on the Fe–Zn alloying reaction.

4. Conclusion

The specific effect of slight variations in the silicon concentration on the Fe–Zn alloying reaction was examined via rapid laser

heating and cooling at various temperatures, which mimics the actual industrial hot-working process. The high spatial and temporal resolution of *in-situ* synchrotron X-ray diffraction alloys confirmed the exact temperatures at which liquid phases appeared and disappeared with respect to silicon content. Slight variations in the temperature did not significantly affect the Fe–Zn alloying reaction. In fact, the Fe–Zn alloying reaction was significantly correlated with the silicon content of the AHSS. The key observations are as follows.

- 1) Initially, a discontinuous nanoscale intermetallic phase appeared in the reacted coating of GI-1.5Si, whereas a thick and continuous intermetallic layer formed at the interface of GI-0Si due to the increase in Fe content in the liquid Zn.
- 2) The nucleation and possibly rapid growth of the Γ Fe–Zn intermetallic phase occurs immediately after the break in the Fe–Al inhibition layer at the coating-steel matrix interface. However, the presence of silicon in the steel substrate suppresses the formation of the Γ Fe–Zn intermetallic phase as the interfacial layer, based on 2D diffractograms; these effects were observed above and below the peritectic temperature (782 °C) in the Fe–Zn binary system.
- 3) The absence of silicon in the steel substrate can create an Fe-rich local environment, leading to a reduction in the amount of residual liquid Zn due to the early formation of the intermetallic (ζ) phase during heating. This also leads to the formation of a uniform and solidified Γ layer, serving as a barrier to prevent direct contact between the liquid Zn and the steel substrate.
- 4) The concentration of silicon in the AHSS substrate significantly affected the Fe–Zn alloying reaction by increasing the amount of liquid Zn and reducing the coverage of intermetallics on the surface, thus resulting in direct contact between liquid Zn and the steel substrate, which may potentially increase the risk of LME.

Credit author statement

S.C. Han: Investigation, Formal analysis, Data curation, Visualization, Writing - original draft. **D.F. Sanchez, D. Grolimund:** Investigation, Resource. **S.-H. Uhm, D.-Y. Choi, H.-C. Jeong:** Conceptualization, Resource, **T.-S. Jun:** Supervision, Conceptualization, Writing - review & editing, Project administration, Funding acquisition.

Declaration of competing interest

The authors declare that they have no known competing financial interests or personal relationships that could have appeared to influence the work reported in this paper.

Data availability

Data will be made available on request.

Acknowledgement

This work was supported by Incheon National University Research Grant in 2019 (2019–0410). The authors wish to acknowledge the Paul Scherrer Institut, Villigen, Switzerland for the provision of beamtime at the microXAS beamline of the Swiss Light Source, the TOMCAT beamline for the provision of the laser heating system and M. Birri for technical support.

References

- [1] B. Joseph, M. Picat, F. Barbier, Liquid metal embrittlement: a state-of-the-art appraisal, *Eur. Phys. J. Appl. Phys.* 5 (1) (1999) 19–31.
- [2] D.G. Kolman, A review of recent advances in the understanding of liquid metal embrittlement, *Corrosion* 75 (1) (2018) 42–57.
- [3] P.J.L. Fernandes, D.R.H. Jones, Mechanisms of liquid metal induced embrittlement, *Int. Mater. Rev.* 42 (6) (1997) 251–261.
- [4] P.J.L. Fernandes, R.E. Clegg, D.R.H. Jones, Failure by liquid metal induced embrittlement, *Eng. Fail. Anal.* 1 (1) (1994) 51–63.
- [5] P. Gordon, H.H., An, the mechanisms of crack initiation and crack propagation in metal-induced embrittlement of metals, *Metall. Trans. A* 13 (3) (1982) 457–472.
- [6] V.Y. Gertsman, S.M. Brummer, Study of grain boundary character along intergranular stress corrosion crack paths in austenitic alloys, *Acta Mater.* 49 (9) (2001) 1589–1598.
- [7] S.P. Lynch, Environmentally assisted cracking: overview of evidence for an adsorption-induced localised-slip process, *Acta Metall.* 36 (10) (1988) 2639–2661.
- [8] B. Alexandreanu, G.S. Was, The role of stress in the efficacy of coincident site lattice boundaries in improving creep and stress corrosion cracking, *Scripta Mater.* 54 (6) (2006) 1047–1052.
- [9] M. Koyama, E. Akiyama, T. Sawaguchi, D. Raabe, K. Tsuzaki, Hydrogen-induced cracking at grain and twin boundaries in an Fe–Mn–C austenitic steel, *Scripta Mater.* 66 (7) (2012) 459–462.
- [10] A. Oudriss, J. Creus, J. Bouhattate, C. Savall, B. Peraudeau, X. Feaugas, The diffusion and trapping of hydrogen along the grain boundaries in polycrystalline nickel, *Scripta Mater.* 66 (1) (2012) 37–40.
- [11] R. Kirchheim, Revisiting hydrogen embrittlement models and hydrogen-induced homogeneous nucleation of dislocations, *Scripta Mater.* 62 (2) (2010) 67–70.
- [12] R. Ashiri, M.A. Haque, C.-W. Ji, M. shamanian, H.R. Salimijazi, Y.-D. Park, Supercritical area and critical nugget diameter for liquid metal embrittlement of Zn-coated twinning induced plasticity steels, *Scripta Mater.* 109 (2015) 6–10.
- [13] R. Ashiri, M. Shamanian, H.R. Salimijazi, M.A. Haque, J.-H. Bae, C.-W. Ji, K.-G. Chin, Y.-D. Park, Liquid metal embrittlement-free welds of Zn-coated twinning induced plasticity steels, *Scripta Mater.* 114 (2016) 41–47.
- [14] M.H. Razmpoosh, E. Biro, D.L. Chen, F. Goodwin, Y. Zhou, Liquid metal embrittlement in laser lap joining of TWIP and medium-manganese TRIP steel: the role of stress and grain boundaries, *Mater. Char.* 145 (2018) 627–633.
- [15] C.W. Lee, D.W. Fan, I.R. Sohn, S.-J. Lee, B.C. De Cooman, Liquid-metal-induced embrittlement of Zn-coated hot stamping steel, *Metall. Mater. Trans. A* 43 (13) (2012) 5122–5127.
- [16] M. Takahashi, M. Nakata, K. Imai, N. Kojima, N. Otsuka, Liquid Metal Embrittlement of Hot Stamped Galvannealed Boron Steel Sheet: Effect of Heating Time on Crack Formation, *ISIJ Int* advpub, 2017.
- [17] D.A.d.C. Ximenes, L.P. Moreira, J.E.R.d. Carvalho, D.N.F. Leite, R.G. Toledo, F.M.d.S. Dias, Phase transformation temperatures and Fe enrichment of a 22MnB5 Zn-Fe coated steel under hot stamping conditions, *J. Mater. Res. Technol.* 9 (1) (2020) 629–635.
- [18] V. Janik, Y. Lan, P. Beentjes, D. Norman, G. Hensen, S. Sridhar, Zn diffusion and α -Fe(Zn) layer growth during annealing of Zn-coated B steel, *Metall. Mater. Trans. A* 47 (1) (2016) 400–411.
- [19] H. Lee, M.C. Jo, S.S. Sohn, S.-H. Kim, T. Song, S.-K. Kim, H.S. Kim, N.J. Kim, S. Lee, Microstructural evolution of liquid metal embrittlement in resistance-spot-welded galvanized TWinning-Induced Plasticity (TWIP) steel sheets, *Mater. Char.* 147 (2019) 233–241.
- [20] S.P. Murugan, K. Mahmud, C. Ji, I. Jo, Y.-D. Park, Critical design parameters of the electrode for liquid metal embrittlement cracking in resistance spot welding, *Weld. World* 63 (6) (2019) 1613–1632.
- [21] C. DiGiovanni, L. He, U. Pistek, F. Goodwin, E. Biro, N.Y. Zhou, Role of spot weld electrode geometry on liquid metal embrittlement crack development, *J. Manuf. Process.* 49 (2020) 1–9.
- [22] A. Ghatei Kalashami, C. DiGiovanni, M.H. Razmpoosh, F. Goodwin, N.Y. Zhou, The effect of silicon content on liquid-metal-embrittlement susceptibility in resistance spot welding of galvanized dual-phase steel, *J. Manuf. Process.* 57 (2020) 370–379.
- [23] A.R. Marder, The metallurgy of zinc-coated steel, *Prog. Mater. Sci.* 45 (3) (2000) 191–271.
- [24] M. Tumuluru, Effect of silicon and retained austenite on the liquid metal embrittlement cracking behavior of GEN3 and high-strength automotive steels, *Weld. J.* 98 (2019) 351s–364s.
- [25] S.-H. Hong, J.-H. Kang, D. Kim, S.-J. Kim, Si effect on Zn-assisted liquid metal embrittlement in Zn-coated TWIP steels: importance of Fe–Zn alloying reaction, *Surf. Coat. Technol.* 393 (2020), 125809.
- [26] A.G. Kalashami, C. DiGiovanni, M.H. Razmpoosh, F. Goodwin, N.Y. Zhou, The role of internal oxides on the liquid metal embrittlement cracking during resistance spot welding of the dual phase steel, *Metall. Mater. Trans. A* 51 (5) (2020) 2180–2191.
- [27] S. Kobayashi, Effects of Si solid solution in Fe substrate on the alloying reaction between Fe substrate and liquid Zn, *ISIJ Int.* 57 (12) (2017) 2214–2219.
- [28] Y. Tobiyama, C. Kato, Effect of the substrate compositions on the growth of Fe–Al interfacial layer formed during hot dip galvanizing, *Tetsu-To-Hagane* 89 (1) (2003) 38–45.
- [29] J.L. Fife, M. Rappaz, M. Pistone, T. Celcer, G. Mikuljan, M. Stampanoni, Development of a laser-based heating system for in situ synchrotron-based X-ray tomographic microscopy, *J. Synchrotron Radiat.* 19 (3) (2012) 352–358.
- [30] W. De Nolf, F. Vanmeert, K. Janssens, XRDUA: crystalline phase distribution maps by two-dimensional scanning and tomographic (micro) X-ray powder diffraction, *J. Appl. Crystallogr.* 47 (3) (2014) 1107–1117.
- [31] F. Perez, B.E. Granger, IPython: a system for interactive scientific computing, *Comput. Sci. Eng.* 9 (3) (2007) 21–29.
- [32] J. Hunter, Matplotlib: a 2D graphics environment, *Comput. Sci. Eng.* 9 (2007) 90–95.
- [33] S.v.d. Walt, S.C. Colbert, G. Varoquaux, The NumPy array: a structure for efficient numerical computation, *Comput. Sci. Eng.* 13 (2) (2011) 22–30.
- [34] K.M. Thyng, C.A. Greene, R.D. Hetland, H.M. Zimmerle, S.F. DiMarco, True colors of oceanography guidelines for effective and accurate colormap selection, *Oceanography* 29 (3) (2016) 9–13.
- [35] Y.S. Touloukian, R.K. Kirby, R.E. Taylor, P.D. Desai, Thermophysical Properties of Matter - the TPRC Data Series, Volume 12. Thermal Expansion Metallic Elements and Alloys. (Reannouncement). Data book, United States, 1975, p. 1443. Medium: X; Size.
- [36] D. Bhattacharya, L. Cho, E. van der Aa, A. Pichler, N. Pottore, H. Ghassemi-Armaki, K.O. Findley, J.G. Speer, Influence of the starting microstructure of an advanced high strength steel on the characteristics of Zn-Assisted liquid metal embrittlement, *Mater. Sci. Eng., A* 804 (2021), 140391.
- [37] C. DiGiovanni, A. Ghatei Kalashami, F. Goodwin, E. Biro, N.Y. Zhou, Occurrence of sub-critical heat affected zone liquid metal embrittlement in joining of advanced high strength steel, *J. Mater. Process. Technol.* 288 (2021), 116917.
- [38] D. Bhattacharya, L. Cho, J. Colburn, D. Smith, D. Marshall, E. van der Aa, A. Pichler, H. Ghassemi-Armaki, N. Pottore, K.O. Findley, J.G. Speer, Influence of selected alloying variations on liquid metal embrittlement susceptibility of quenched and partitioned steels, *Mater. Des.* 224 (2022), 111356.
- [39] W. Dong, K. Ding, H. Pan, M. Lei, L. Wang, Y. Gao, Role of Si content in the element segregation of galvanized QP980 advanced high strength steel, *J. Occup. Med.* 74 (6) (2022) 2369–2376.
- [40] P. Brown, The structure of the δ -phase in the transition metal-zinc alloy systems, *Acta Crystallogr.* 15 (6) (1962) 608–612.
- [41] M.H. Hong, H. Saka, Transmission electron microscopy of the iron-zinc δ 1 intermetallic phase, *Scripta Mater.* 36 (12) (1997) 1423–1429.
- [42] C.H.E. Belin, R.C.H. Belin, Synthesis and crystal structure determinations in the Γ and δ phase domains of the iron–zinc system: electronic and bonding analysis of Fe13Zn39 and FeZn10, a subtle deviation from the hume–rothery standard? *J. Solid State Chem.* 151 (1) (2000) 85–95.
- [43] A.S. Koster, J.C. Schoone, Structure of the cubic iron–zinc phase Fe22Zn78, *Acta Crystallogr. B* 37 (10) (1981) 1905–1907.
- [44] L. Cho, M.S. Kim, Y.H. Kim, B.C. De Cooman, Influence of gas atmosphere dew point on the galvannealing of CMnSi TRIP steel, *Metall. Mater. Trans. A* 44 (11) (2013) 5081–5095.
- [45] M.S. Kozdras, P. Niessen, Silicon-induced destabilization of galvanized coatings in the sandelin peak region, *Metallography* 22 (3) (1989) 253–267.
- [46] C. Sha, S. Liu, Y. Du, H. Xu, L. Zhang, Y. Liu, Experimental investigation and thermodynamic reassessment of the Fe–Si–Zn system, *Calphad* 34 (4) (2010) 405–414.
- [47] X. Su, N.-Y. Tang, J.M. Toguri, 450 °C isothermal section of the Fe–Zn–Si ternary phase diagram, *Can. Metall. Q.* 40 (3) (2001) 377–384.
- [48] X. Su, F. Yin, Z. Li, N.-Y. Tang, M. Zhao, Thermodynamic calculation of the Fe–Zn–Si system, *J. Alloys Compd.* 396 (1) (2005) 156–163.
- [49] A. Faghri, Y. Zhang, Fundamentals of Multiphase Heat Transfer and Flow, 2020.
- [50] S. Jeon, T. Heo, S.-Y. Hwang, J. Ciston, K.C. Bustillo, B.W. Reed, J. Ham, S. Kang, S. Kim, J. Lim, K. Lim, J.S. Kim, M.-H. Kang, R.S. Bloom, S. Hong, K. Kim, A. Zettl, W.Y. Kim, P. Ercius, J. Park, W.C. Lee, Reversible disorder-order transitions in atomic crystal nucleation, *Science* 371 (6528) (2021) 498–503.